AGU PUBLICATIONS

Geophysical Research Letters

RESEARCH LETTER
10.1002/2014GL061226

Key Points:
- Internal waves suffer PSI and then break down to turbulence through convective instability
- Turbulence energetics and phasing during beam refraction has been quantified
- Subharmonics, turbulence, and harmonics substantially weakens the beam that is reflected from the pcynocline similar to observations at Kaena Ridge

Correspondence to:
S. Sarkar,
sarkar@ucsd.edu

Citation:
Gayen, B., and S. Sarkar (2014), PSI to turbulence during internal wave beam refraction through the upper ocean pycnocline, *Geophys. Res. Lett.*, *41*, 8953–8960, doi:10.1002/2014GL061226.

Received 15 JUL 2014
Accepted 20 NOV 2014
Accepted article online 25 NOV 2014
Published online 16 DEC 2014

PSI to turbulence during internal wave beam refraction through the upper ocean pycnocline

B. Gayen[1] and S. Sarkar[2]

[1]Research School of Earth Science, Australian National University, Canberra, ACT, Australia [2]Mechanical and Aerospace Engineering Department, University of California, San Diego, La Jolla, California, USA

Abstract A numerical study based on large eddy simulation (LES) is performed to investigate the nonlinear interaction of a semidiurnal (M2) internal wave beam with an upper ocean pycnocline. During refraction through the pycnocline, the wave beam undergoes parametric subharmonic instability (PSI) with formation of waves with (1/2)M2 frequency. The three-dimensional LES enables new results that quantify the route to turbulence through PSI. The subharmonic waves generated from PSI have an order of magnitude smaller vertical scale and are susceptible to wave breaking. Convective instability initiates transition to turbulence, while shear production maintains it. Turbulence at points in the subharmonic wave paths is modulated at (1/2)M2 frequency. The beam suffers substantial degradation owing to PSI, reflected harmonics and ducted waves so that only about 30% of the incoming energy is transported by the main reflected beam.

1. Introduction

Internal waves generated by the surface tide flowing over rough topography propagate into the ocean interior where they may break down into turbulence, thus playing a key role in ocean mixing [*Munk and Wunsch*, 1998; *St. Laurent and Garrett*, 2002]. Generation at critical or supercritical sites leads to the formation of propagating internal wave (IW) beams. Observational studies [*Martin et al.*, 2006; *Cole et al.*, 2009; *Holbrook et al.*, 2009; *Johnston et al.*, 2011] show that IW beams form and then degrade upon interaction with a pycnocline but the mechanisms underlying the degradation are not well understood.

A single internal wave of frequency ω_0 and wave vector $\mathbf{k}_0$ is subject to the parametric subharmonic instability (PSI) under certain circumstances whereby the primary wave decays by transferring energy into two waves of lower frequency, such that $\mathbf{k}_0 = \mathbf{k}_1 + \mathbf{k}_2$ and $\omega_0 = \omega_1 + \omega_2$ are satisfied. In previous work [*Gayen and Sarkar*, 2013], we showed using 2-D simulations that PSI can occur when an incident IW beam refracts through the nonuniform stratification of the upper-ocean pycnocline. In that parametric study, it was found that incoming waves suffered PSI as long as the wave amplitude was sufficiently large for nonlinear behavior and the pycnocline was sufficiently thick to accommodate 1–2 wavelengths of the subharmonic waves. However, owing to the two-dimensional approximation, we could not address the important question of turbulence and mixing that is potentially present during the IW beam refraction. Here we perform high-resolution, three-dimensional LES that charts the route to turbulence from PSI and adds another degree of realism to numerical modeling of the internal wave dynamics.

Direct transfer through PSI has been observed; e.g., from semidiurnal to diurnal motions in the vicinity of Kaena Ridge [*Carter and Gregg*, 2006; *Sun and Pinkel*, 2013], and from the internal tide to near-inertial motions near 29°N [*MacKinnon et al.*, 2013]. Downward propagating IW beams, after generation at a continental shelf break, have been found to suffer PSI in two-dimensional simulations by *Gerkema et al.* [2006]. In a laboratory experiment [*Clark and Sutherland*, 2010], large-amplitude oscillation of a cylinder led to IW beams that became unstable to PSI. There is a large body of literature on PSI, e.g., as discussed in recent contributions [*Bourget et al.*, 2013; *Gayen and Sarkar*, 2013]. It has been hypothesized that PSI is effective as a route to turbulence from oceanic internal waves. However, demonstration that internal waves cascade to three-dimensional turbulence through PSI has proved elusive in measurements and numerical simulations because of the broad range of spatiotemporal scales. This motivates the present work.

Table 1. Simulation Parameters

Physical Parameters		
Vertical thickness of IW beam	l_b (m)	100
Vertical thickness of pycnocline	l_{py} (m)	50
Relative thickness of IW beam	l_b/l_{py}	2
Velocity of IW beam	u_0 (cm/s)	0.41
Frequency of IW beam	Ω (s^{-1})	1.4×10^{-4}
Deep stratification	N_1 (s^{-1})	1.15×10^{-3}
Pycnocline inhomogeneity	$\Gamma = N_2/N_1$	4
Incoming IW angle	θ (°)	7
Molecular viscosity	ν (m^2/s)	10^{-6}
Prandtl number	$Pr = \nu/\kappa$	7
Froude number	$Fr = u_0/(N_1 l_b)$	0.035
Reynolds number	$Re = u_b l_b/\nu$	4.1×10^5

2. Problem Setup

Large-eddy simulation (LES) is used to obtain the filtered velocity and density fields by numerical solution of the Navier-Stokes equations under the Boussinesq approximation, written in Cartesian coordinates $[x, y, z]$ in dimensional form as follows:

$$\nabla \cdot \mathbf{u} = 0$$
$$\frac{D\mathbf{u}}{Dt} = -\frac{1}{\rho_0}\nabla p^* + \nu\nabla^2\mathbf{u} - \nabla \cdot \boldsymbol{\tau}$$
$$\frac{D\rho^*}{Dt} = \kappa\nabla^2\rho^* - w\frac{\mathrm{d}\rho^b}{\mathrm{d}z} - \nabla \cdot \lambda \quad (1)$$

Here p^* and ρ^* denote *deviation* from the background pressure (p_b) and density (ρ_b), respectively. The total density, denoted by ρ, is equal to $\rho^* + \rho_b$. The present problem is motivated by internal waves measured at Kaena Ridge, south of the critical latitude of 29°N for the M2 internal tide, so that the subharmonic M2/2 in the observations [*Carter and Gregg*, 2006; *Sun and Pinkel*, 2013] has sufficient separation from the inertial frequency. Coriolis effects are not dominant on internal wave stability at such low latitudes, and therefore, rotation is not included in the model for simplicity.

The quantity $\boldsymbol{\tau}$ that denotes the subgrid-scale stress tensor and λ that is the subgrid density flux are modeled as described by *Gayen et al.* [2010]. Briefly, $\boldsymbol{\tau}$ is represented with a dynamic eddy viscosity model and λ with a dynamic eddy diffusivity model. Each subgrid model has a corresponding Smagorinsky coefficient that is evaluated through a dynamic procedure. Spanwise derivatives are treated with a pseudo-spectral method, and the wall normal spatial derivatives are computed with second-order finite differences. A third-order Runge-Kutta method is used for time stepping, and viscous terms are treated implicitly with the Crank-Nicolson method. The test domain, excluding the sponge region, consists of a rectangular box of 3000 m length, 300 m height, and 60 m width with a $2300 \times 128 \times 500$ grid, having x and z stretching. The grid spacing ($\Delta x_{\min} = 0.5$ m, $\Delta x_{\max} = 1.5$ m, $\Delta z_{\min} = 0.25$ m, $\Delta z_{\max} = 1$ m, $\Delta y = 0.5$ m) is sufficient to resolve smaller waves generated during the subharmonic instability. Grid spacing is determined to be sufficient for LES by examining the spanwise spatial spectra and temporal spectra. Variable time stepping with a fixed Courant-Friedrichs-Lewy number of 1.2 is used which gives time step, $\Delta t \simeq 1$ s. The present simulation takes approximately 16,000 CPU hours to simulate one tidal cycle, and we simulate 32 cycles which include the initial 6 cycles for arrival of the mean beam into the pycnocline, the following 14 cycles for the formation of subharmonics, higher harmonics, and transition to turbulence, and the final 10 cycles for turbulence to reach a quasi steady state.

The present configuration is similar to *Gayen and Sarkar* [2013], where the IW beam is forced at the left-hand side of the computational domain using the analytical value of the parallel and transverse velocity components, as well as the buoyancy fields of the Thomas-Stevenson profiles [*Thomas and Stevenson*, 1972; *Mercier et al.*, 2010]. At the top of the domain, a free surface condition with the rigid-lid approximation is imposed with zero gradient value for the density. The right and bottom boundaries are artificial boundaries corresponding to the truncation of the domain. Rayleigh damping or a sponge layer is used at the right and the bottom of computational domain so as to minimize spurious reflections from the artificial boundary into the test section of the computational domain. The sponge region at the right boundary contains 25 points and extends from 3000 m to 3500 m, while the bottom sponge with 15 points extends from $z = -180$ m to -250 m. The strength of the sponge region was adjusted until reflection from the IW beams incident on the sponge was found to be negligible.

The parameters correspond to case A5 of *Gayen and Sarkar* [2013] and are summarized in Table 1. Under the conditions of the background stratification chosen here, the IW beam is stable during propagation until it encounters variable stratification (upper ocean pycnocline).

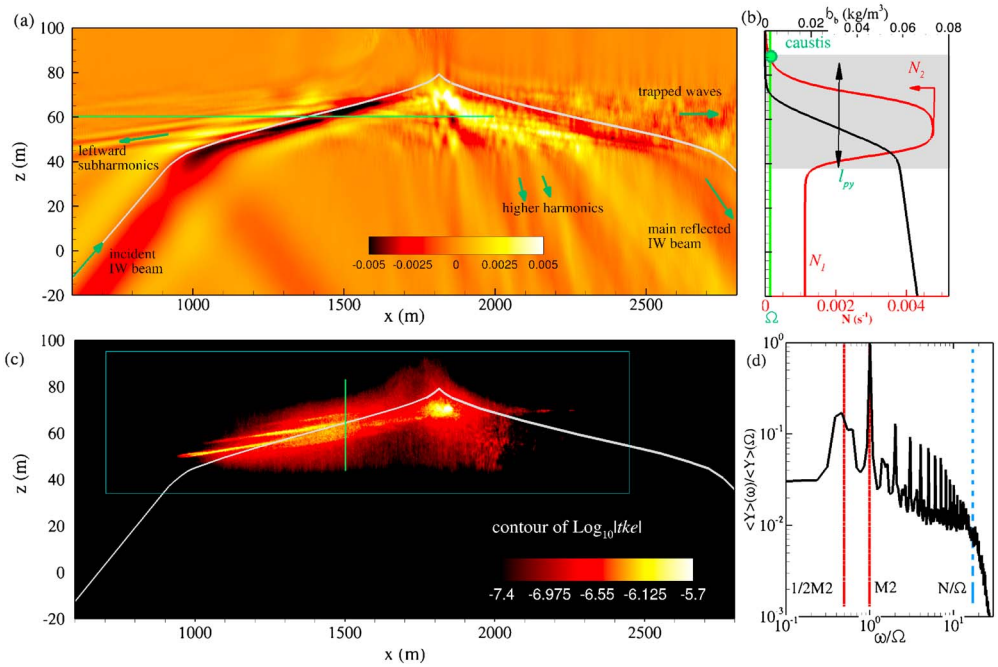

Figure 1. (a) A vertical x-z snapshot of the streamwise velocity, $u(x,z)$ m/s, at $t = 30\ T$. The beam path is denoted by the white line. The snapshot shows a portion of the computational x-z domain. (b) Profiles of the background density difference, $\rho_b(z)$, kg/m^3 with respect to a reference density and buoyancy frequency, $N(z)$ s^{-1}, where N_1 and N_2 are the buoyancy frequency in the lower part of the domain and at the pycnocline center, respectively. (c) Contour of turbulent kinetic energy (m^2/s^2) at $t = 30\ T$. The boxed region is used for area integration of terms in TKE budget. Turbulence data at the vertical green line will be discussed later in Figure 4. (d) Line-averaged power spectrum $\langle Y\rangle(\omega)$, normalized by its value at the M2 frequency, of streamwise beam velocity measured inside the pycnocline. The time series is taken over a time interval of 20 T and at the green horizontal line in Figure 1a at location $z = 60$ m extending from $x = 500$ m to $x = 2000$ m.

3. Results

3.1. Transition to Turbulence

An upward and rightward traveling IW beam encounters the upper ocean pycnocline at $x \sim 1000$ m and $z \sim 50$ m and refracts through the pycnocline as shown in Figure 1a. The IW beam narrows (vertical wave number increases) during transmission through the lower transition layer, $N_1 \rightarrow N_2$, where N_2 is larger than N_1. The beam also refracts rightward and finally reflects from a caustic (IW frequency equal to buoyancy frequency) at $z \sim 85$ m. It returns back to the deep ocean after traveling through the transmission layer. The IW beam behaves linearly prior to $t \sim 15\ T$. Later, harmonics of the fundamental and resonant subharmonics form [*Gayen and Sarkar*, 2013].

After time $t \sim 15\ T$, during refraction through the pycnocline, the incoming IW beam becomes nonlinear and susceptible to PSI. Figure 1d shows the temporal spectrum of the velocity signal measured at the green horizontal line in Figure 1a that encompasses the refracted and reflected wave regions. The temporal spectrum is obtained by an x average of the time-to-frequency transform of $u(x,t)$ at points on the green horizontal line. There is clear evidence of the energy peak at $\omega \sim 0.5\Omega$ in addition to the primary peak at the wave forcing frequency, Ω. Harmonics of M2 including a strong spectral peak at M4 and interharmonics are associated with the reflected wave signal and not the refracted incident wave. The signature of PSI is also evident in physical space. One of the two participating subharmonic waves has horizontal wave number with sign opposite to that of the primary wave resulting in spontaneous generation of leftward moving waves which are spotted inside the pycnocline and at the left side of the main IW beam. A detailed discussion of the characteristics of these subharmonic waves and their growth rate is given by *Gayen and Sarkar* [2013]. Briefly, the spectrum shows a subharmonic peak at $\omega \simeq 0.5\omega_0$ associated with a pair of oppositely traveling daughter waves. The incident 7° IW beam refracts through the pycnocline, attains a shallower angle of approximately 2.4°, and subsequently suffers PSI. The analysis of *Bourget et al.* [2013]

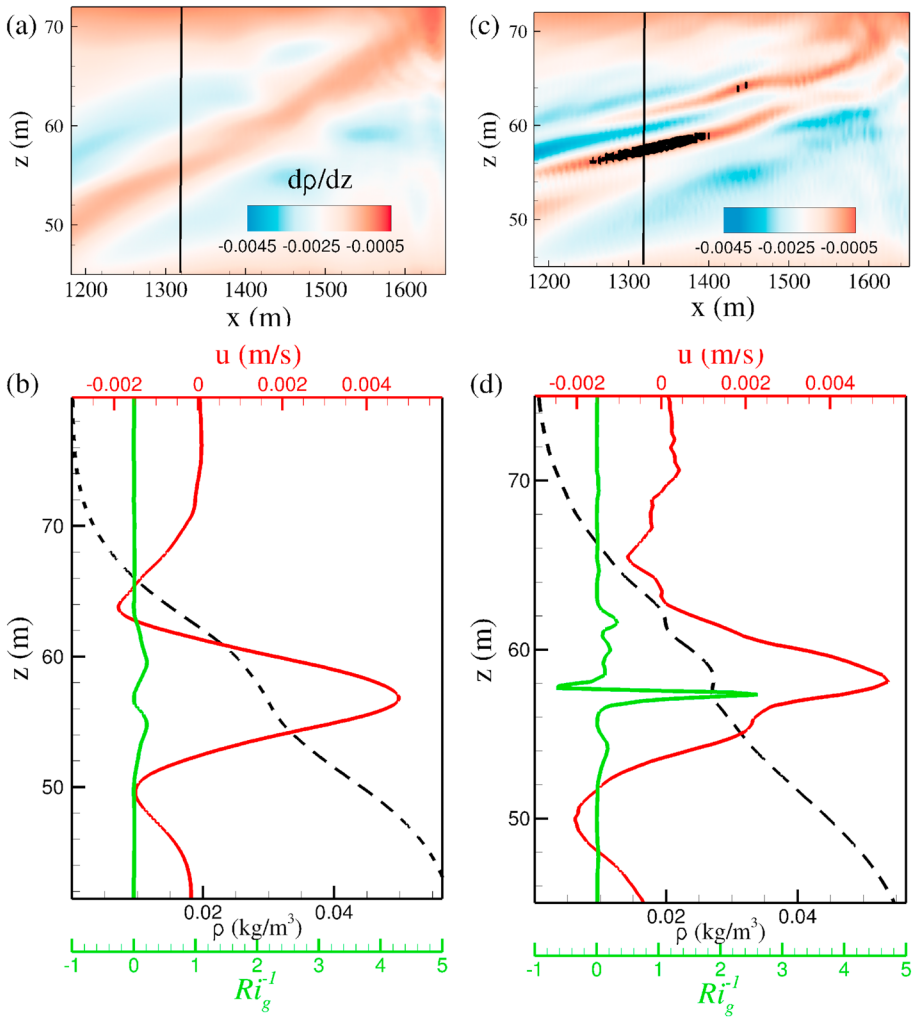

Figure 2. (a) Density gradient, $\partial\rho/\partial z(x,z)$ kg/m^4, at a small section of the IW beam inside the pycnocline at $t = 14\,T$, *before* the subharmonic instability. (b) Profiles correspond to the streamwise velocity, $u(z)$ m/s, density, $\rho(z)$ kg/m^3, and inverse gradient Richardson number, $(Ri_g)^{-1}(z)$ along the vertical black line marked in Figure 2a at same time instant. Similarly, profiles in Figure 2d correspond to the vertical black line in Figure 2c. (c and d) Analogs of Figures 2a and 2b at a later time $t = 18\,T$, *after* PSI is established. The black contour in Figure 2c shows a region with positive density gradient and negative Ri_g^{-1}.

shows that PSI results in a pair of subharmonic peaks that asymptotically merge, i.e., $\omega_{1,2} \rightarrow 0.5\omega_0$ as the wave Reynolds number, $Re \rightarrow \infty$. For the present finite (but large) Re, spectral peaks are at $\omega_1 \simeq 0.53\omega_0$ and $\omega_2 \simeq 0.47\omega_0$ and where ω_0 is the fundamental M2 frequency, Ω. Analysis of the space-time data obtained after band passing at ω_0, ω_1 and ω_2 gives the phase velocities and thus the wave numbers. We find that the wave numbers form a triad: the fundamental has $k_{x,0} \simeq 0.012$ m^{-1}, $k_{z,0} \simeq -0.29$ m^{-1}, while the secondary waves have $k_{x,1} \simeq 0.065$ m^{-1}, $k_{z,1} \simeq -3.03$ m^{-1}, and $k_{x,2} \simeq -0.055$ m^{-1}, $k_{z,2} \simeq 2.77$ m^{-1}, respectively. Because of their small vertical wavelength ($\simeq$ 2 m), an order of magnitude smaller than the parent refracted wave, the daughter waves potentially drive further instability by significantly decreasing the density gradient and increasing velocity shear as will be demonstrated. Figure 1c shows the spatial distribution of turbulence by plotting the turbulent kinetic energy (TKE) denoted by $K = 1/2\langle u_i' u_i' \rangle$, where $u_i' = u_i - \langle u_i \rangle$. Mean (bracketed) values are evaluated by spanwise (y) averaging, and fluctuations (primes) are deviations from the mean.

Figure 2a shows the vertical gradient of the density at $t = 14\,T$ before PSI. The internal wave is linear and the beam exhibits stable values of gradient Richardson number ($Ri_g = N^2/S^2$, where N and S are the local values of mean buoyancy frequency and mean shear, respectively) across the IW beam as shown in Figure 2b. During PSI, the profiles of the velocity and density show presence of small scales with a local

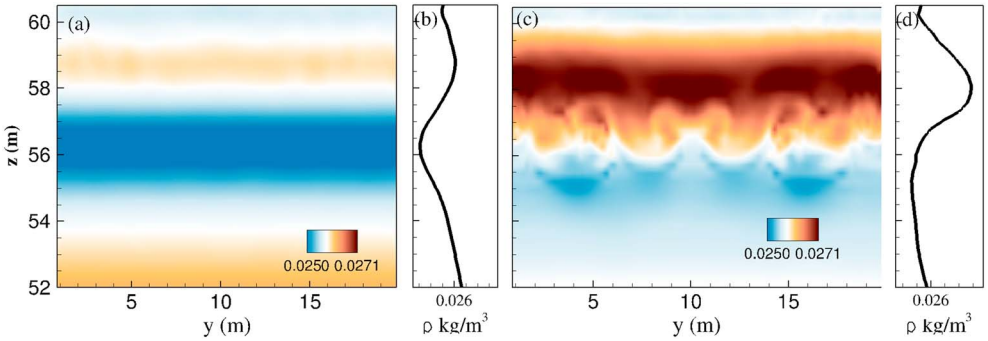

Figure 3. Vertical y-z slices of the density, $\rho(y,z)$ kg/m^3, field at $x = 1320$ m during the PSI event. (a) Density inversion at $t = 18.1\ T$ and (b) mean density profile at that time. (c) Mushroom structures that form at $t = 18.11\ T$, immediately after the density inversion, and (d) the corresponding mean density profile.

increase of S and decrease of N that combine to increase Ri_g^{-1}. Ultimately, thin convectively unstable regions with $\partial\rho/\partial z > 0$ and $Ri_g^{-1} < 0$ form in the subharmonics as shown in Figures 2c and 2d.

The first density inversion (Figure 3a) is noticed inside the pycnocline at a location $x = 1320$ m, extending over the region $57 < z < 59$ m, which is comparable in thickness to the wavelength of PSI-generated waves. Soon after, a mushroom-shaped plume (Figure 3b) forms, suggesting convective rather than shear instability. Several turbulent patches are subsequently initiated at the beam in the pycnocline, similarly by convective instability.

3.2. Internal Wave Energetics

The partition of the main incoming IW beam energy ($\mathcal{F}_{\text{beam,in}} = 100\%$) into its component waves during the interaction with the pycnocline is quantified by computing the wave flux (pressure-velocity correlation). The leftward flux is computed at the vertical line between (x,z) locations of (500 m, 20 m) and (500 m, 150 m), the rightward flux at a vertical line between (3000 m, 20 m) and (3000 m, 150 m), and the bottom flux at a horizontal line at $z = 0$ that extends between $x = 1100$ m and 3000 m. We also utilize the fact that the component waves have different propagation angles and intersect the boundaries at different, known locations. The wave flux associated with leftward going subharmonics is $\mathcal{F}_{\text{sub,left}} \approx 10\%$, the main reflected IW beam carries $\mathcal{F}_{\text{beam,out}} \approx 31\%$, the rightward, horizontal flux ducting through the pycnocline via solitary waves and trapped subharmonics is $\mathcal{F}_{\text{pyc,right}} \approx 15\%$, and $\mathcal{F}_{\text{bottom}} \approx 35\%$ is associated with waves that escape from the bottom boundary in the form of higher harmonics, subharmonics, and the immediate reflection of IW beam upon encountering the lower boundary of the pycnocline. Since the leftward subharmonic carries 10% energy, and assuming that, the rightward subharmonic also carries approximately 10% gives a net 20% energy loss through PSI.

3.3. Turbulence

We now turn to the temporal evolution of turbulence statistics by illustrating the behavior at the vertical green line at $x = 1500$ m in Figure 1c.

Figure 4a shows the evolution of density at different elevations starting from $z = 54$ m to $z = 65.5$ m. The circles in Figure 4a show instances where the density traces at different heights become tangent or even cross, indicating convective instability. These instances of near-zero density difference at a *fixed* location occur every *two* cycles. For example, the near-zero density difference at density $\rho \approx 0.035$ kg/m^3 corresponding to location $z \sim 55$ m occurs at $t = 322$ h and $t = 346$ h with interval close to 24.8 h, which is twice the M2 time period. The wavefield modulates the background density so that N^2 at any given spatial location achieves a local minimum when the perturbation density gradient $(\partial\rho'/\partial z)$ attains its positive maximum, an event that occurs once a cycle, i.e., at time interval of $T = 12.4$ h. Indeed, at the location $z \sim 55$ m, local minima in N^2 can be seen at period T but the occurrence of near-zero N^2 (convective instability) at that location occurs at period $2\ T$, corresponding to the subharmonic and not the primary wave period. It is the subharmonic wave with M2/2 frequency whose perturbation density gradient is sufficiently large to cause convective instability.

The phasing of the convective instability relative to the baroclinic velocity is also of interest. The streamwise velocity over the same region is plotted in Figure 4b. The circled regions in Figure 4a occur when the flow

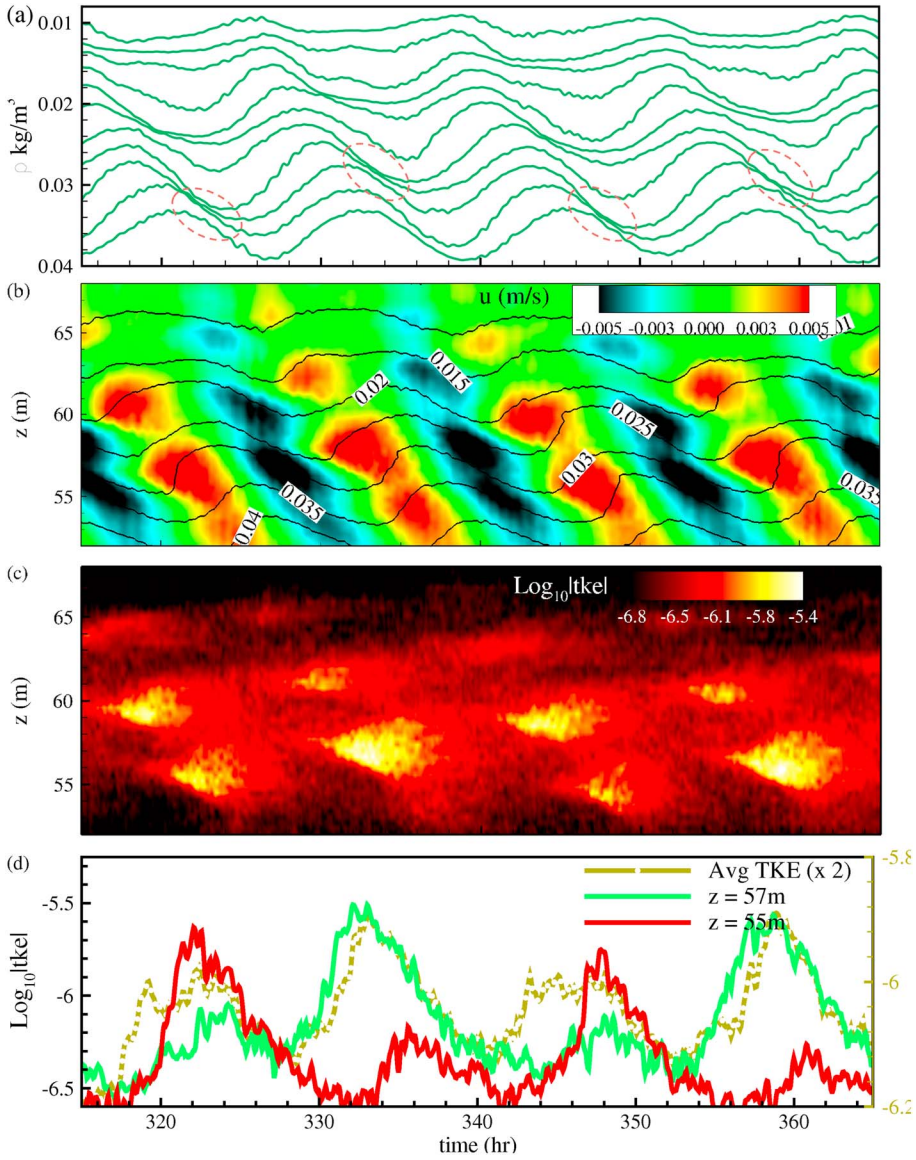

Figure 4. (a) Time evolution of density, ρ (kg/m^3), at different heights, with the bottom line (highest density) corresponding to the smallest elevation, $z = 54$ m, and the top one to $z = 65.5$ m. Circles locate events of reduced (near-zero) density gradient. (b) Temporal evolution of mean streamwise velocity (m/s) and isopycnals (black lines). (c) Temporal evolution of TKE (m^2/s^2) profile. (d) Temporal evolution of TKE at locations $z = 55$ m, $z = 57$ m, and TKE averaged over a vertical line. Data taken at $x = 1500$ m, green vertical line in Figure 1c.

velocity reverses from negative to positive through the zero velocity point. This is due to the fact that, in a linear wave, the density lags the vertical velocity by $\pi/2$ and, since the vertical and horizontal fluid velocity have the same sign in the present problem, it also lags the horizontal velocity by $\pi/2$.

Due to the combined effect of density and velocity, the turbulent kinetic energy (TKE) shows significant vertical variability over the tidal cycle. Inside the pycnocline, patches of enhanced TKE are observed along the subharmonic wave paths and approximately separated by their vertical wave length, which is also clear from the overall spatial view of the TKE in Figure 1c. Figure 4c shows multiple TKE patches, e.g., at locations $z \sim 55$, 60, and 65 m, that occur at the same $z - t$ locations as the near-zero density gradients that were seen in Figure 4a. These TKE patches repeat at the temporal period of the M2/2 frequency subharmonic. Patches of TKE at locations $z \sim 62.5$ and $z \sim 57$ m, associated with breaking of different PSI waves, are offset in time with respect to the three previously described TKE patches and also repeat with the $M2/2$ subharmonic frequency. The evolution of TKE at fixed points and the TKE averaged over a vertical line are shown

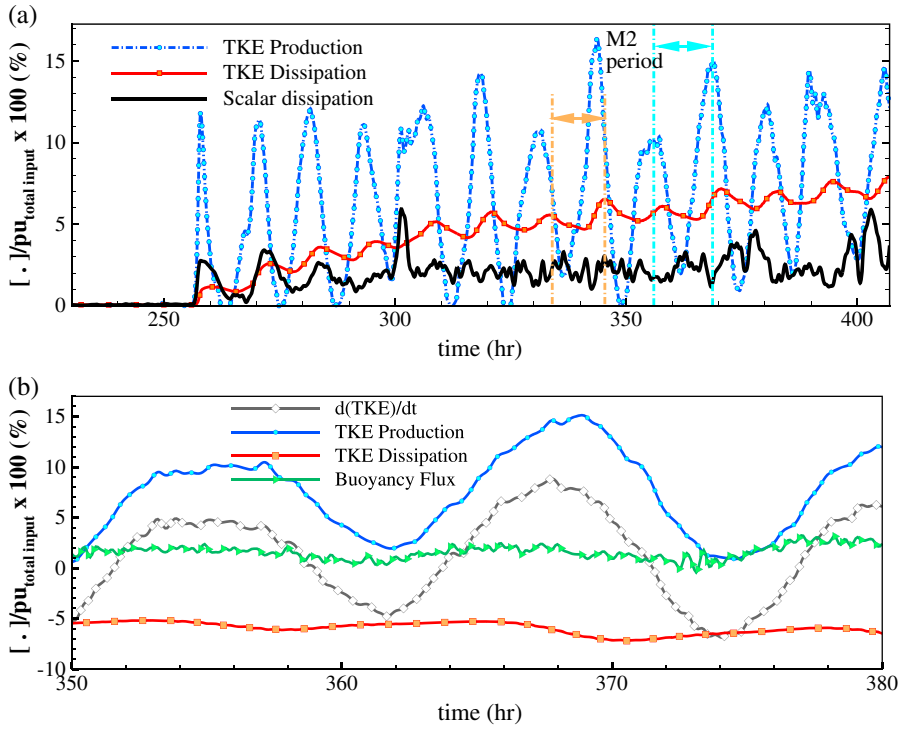

Figure 5. (a) Cycle evolution of area-integrated values of the quantities, normalized by the incoming wave flux, in TKE budget along with integrated scalar dissipation. Area of integration is chosen to capture the entire region of turbulence and is marked by the green rectangle in Figure 1c. The M2 period of the area-integrated production and dissipation rate are shown with cyan and orange lines, respectively. (b) The budget of integrated TKE over two M2 cycles.

in Figure 4d. At a given location, the maximum of TKE repeats at M2/2 temporal frequency, for instance, TKE at $x = 55$ m exhibits peaks at $t = 323$ h and $t = 348$ h while there are auxiliary local maxima at $t = 326$ h and $t = 361$ h. On the other hand, the line-averaged TKE shows M2 temporal frequency since peaks in the temporal evolution at different spatial locations on the vertical line occur with a temporal offset, e.g., TKE peaks at $z = 55$ m are temporally offset with respect to $z = 57$ m in Figure 4d.

Figure 5a shows the temporal evolution of integrated values of terms in the TKE budget. The integration is over the rectangular box in Figure 1c. Here each turbulent quantity is normalized by the input internal wave flux $\int \mathrm{pu}_{x=0}\,\mathrm{d}z$. The spatially integrated turbulence becomes nonnegligible at $t \sim 256$ h. Although each turbulent event is initiated by convective instability, it is *shear production* that *maintains* TKE. Unlike the half-M2 temporal frequency of peak TKE at a given z location, the integrated shear production, $\int \langle P \rangle \mathrm{d}V$ peaks with M2 temporal frequency. This difference between M2/2 frequency of local and M2 frequency of spatially integrated statistics occurs because spatial integration captures turbulence from the breaking of PSI waves at multiple locations along the IW beam. Integrated turbulent dissipation, $\int \langle \varepsilon \rangle \mathrm{d}V$, also shows modulation at *M2* frequency. Interestingly, turbulence in the pycnocline (quantified by turbulent dissipation rate here and by line-averaged TKE in Figure 4d) is present through the tidal cycle, albeit with M2 modulation. Both $\int \langle P \rangle \mathrm{d}V$ and $\int \langle \varepsilon \rangle \mathrm{d}V$ are $\mathcal{O}(10)$% of the total input wave flux. Figure 5b shows the dominance of shear production in the TKE budget. Patches of positive buoyancy flux, essential for transition to turbulence, are locally present but adjacent negative values lead to a small spatially integrated value.

Dissipation of the turbulent potential energy $\langle \varepsilon_\rho \rangle$ has been calculated, and the spatially integrated value is shown as a function of time along with TKE production and dissipation in Figure 5. Here $\epsilon_\rho = 1/2N^2 \chi / (\mathrm{d}\rho_b/\mathrm{d}z)^2$, and the scalar dissipation is $\chi = 2\kappa \langle \partial\rho'/\partial x_k \partial\rho'/\partial x_k \rangle$. Variation over the tidal cycle of $\int \langle \varepsilon_\rho \rangle \mathrm{d}V$ is not systematic. Scalar mixing in the present problem can be characterized in terms of a turbulent mixing efficiency defined as $\int \langle \varepsilon_\rho \rangle \mathrm{d}V / \int \langle \varepsilon \rangle \mathrm{d}V$. The mixing efficiency, thus defined, is found to be $\eta \sim 30\%$. The turbulent eddy diffusivity $\kappa_\rho = |\langle w'\rho' \rangle / d\langle \rho \rangle / \mathrm{d}z|$ has also been calculated. The value of κ_ρ is enhanced to $\mathcal{O}(10^3)$ relative to the molecular value.

4. Conclusions

We perform high-resolution, three-dimensional LES to demonstrate that oceanic high-mode internal waves are susceptible to nonlinear breakdown through PSI and eventually to small scale turbulence when they refract through the variable stratification of a pycnocline. Coriolis effects are not included in the model which is thus limited to examination of wave instability at low latitudes, equatorward relative to the critical latitude (29°N) for M2 internal tide propagation. Refraction decreases the vertical length scale of the incident IW beam, PSI of the refracted wave generates subharmonics with a further order of magnitude reduction of vertical scale, and finally, wave steepening develops into three-dimensional turbulence via convective instability. Although turbulence at a given location is initiated through convective instability, it is maintained mainly by shear production and is continuously drained through viscous dissipation. Elevated turbulence is observed predominantly along the subharmonic wave paths in the pycnocline with temporal frequency half of the M2 tidal frequency at any fixed location inside these wave paths. Line and volume-averaged turbulence statistics show contributions from different breaking regions leading to temporal modulation at M2 frequency. The eddy diffusivity is enhanced to as large as 500 times the molecular value and the mixing efficiency is $\eta \sim 30\%$.

The present work examines transition to turbulence and turbulence properties in a quasi-steady regime through a computationally expensive three-dimensional simulation conducted over a long time (30 periods). Here an internal wave beam with Froude number, $Fr = 0.035$, and vertical thickness, $l_b = 100$ m, propagates at 7° into a pycnocline of thickness, $l_{py} = 50$ m. In our previous parametric study [*Gayen and Sarkar*, 2013], we demonstrated that PSI occurred as long as the pycnocline was not too thin ($l_{py}/l_b > 0.1$ so that the vertical extent of the pycnocline can support 1–2 wavelengths of the M2/2 subharmonic) and the wave amplitude is not too small (*Fr* exceeds approximately 0.015). All of the cases exhibiting PSI also show breakdown to turbulence but, owing to the computational expense, we defer parametric examination of the turbulence characteristics with additional high-resolution, long-time simulations to a future paper.

There is substantial degradation of the internal wave beam when it interacts with the pycnocline with only about 30% of the incoming wave energy carried by the main reflected beam. The present results may thus help explain previous observations [*Martin et al.*, 2006; *Cole et al.*, 2009; *Johnston et al.*, 2011] that the energetic internal wave beams emanating from topographic generation sites attenuate after interaction with the upper ocean pycnocline.

Acknowledgments

We are pleased to acknowledge support through ONR N000140910287, program manager Terri Paluszkiewicz, ARC DECRA Fellowship DE140100089 for B.G., and helpful discussions with Shaun Johnston, SIO. Model output can be obtained through a written request to the corresponding author.

The Editor thanks three anonymous reviewers for their assistance in evaluating this paper.

References

Bourget, B., T. Dauxois, S. Joubaud, and P. Odier (2013), Experimental study of parametric subharmonic instability for internal plane waves, *J. Fluid Mech.*, *723*, 1–20.

Carter, G. S., and M. C. Gregg (2006), Persistent near-diurnal internal waves observed above a site of M2 barotropic-to-baroclinic conversion, *J. Phys. Oceanogr.*, *36*, 1136–1147.

Clark, H. A., and B. R. Sutherland (2010), Generation, propagation and breaking of an internal wave beam, *Phys. Fluids*, *22*, 076601.

Cole, S. T., D. L. Rudnick, B. A. Hodges, and J. P. Martin (2009), Observations of tidal internal wave beams at Kauai Channel, Hawaii, *J. Phys. Oceanogr.*, *39*, 421–436.

Gayen, B., and S. Sarkar (2013), Degradation of an internal wave beam by parametric subharmonic instability in an upper ocean pycnocline, *J. Geophys. Res. Oceans*, *118*, 4689–4698, doi:10.1002/jgrc.20321.

Gayen, B., S. Sarkar, and J. R. Taylor (2010), Large eddy simulation of a stratified boundary layer under an oscillatory current, *J. Fluid Mech.*, *643*, 233–266.

Gerkema, T., C. Staquet, and P. Bouruet-Aubertot (2006), Decay of semi-diurnal internal-tide beams due to subharmonic resonance, *Geophys. Res. Lett.*, *33*, L08604, doi:10.1029/2005GL025105.

Holbrook, W. S., I. Fer, and R. W. Schmitt (2009), Images of internal tides near the Norwegian continental slope, *Geophys. Res. Lett.*, *36*, L00D10, doi:10.1029/2009GL038909.

Johnston, T. M. S., D. L. Rudnick, G. S. Carter, R. E. Todd, and S. T. Cole (2011), Internal tidal beams and mixing near Monterey Bay, *J. Geophys. Res.*, *116*, C03017, doi:10.1029/2010JC006592.

MacKinnon, J. A., M. H. Alford, O. Sun, R. Pinkel, Z. Zhao, and J. Klymak (2013), Parametric subharmonic instability of the internal tide at 29°N, *J. Phys. Oceanogr.*, *43*, 17–28.

Martin, J. P., D. L. Rudnick, and R. Pinkel (2006), Spatially broad observations of internal waves in the upper ocean at the Hawaiian Ridge, *J. Phys. Oceanogr.*, *36*, 1085–1103.

Mercier, M. J., D. Martinand, M. Mathur, L. Gostiaux, T. Peacock, and T. Dauxois (2010), New wave generation, *J. Fluid Mech.*, *657*, 308–334.

Munk, W., and C. Wunsch (1998), Abyssal recipes II: Energetics of tidal and wind mixing, *Deep Sea Res., I*, *45*, 1977–2010.

Thomas, N. H., and T. N. Stevenson (1972), A similarity solution for viscous internal waves, *J. Fluid Mech.*, *54*, 495–506.

St. Laurent, L., and C. Garrett (2002), The role of internal tides in mixing the deep ocean, *J. Phys. Oceanogr.*, *32*, 2882–2899.

Sun, O., and R. Pinkel (2013), Subharmonic energy transfer from the semidiurnal internal tide to near-diurnal motions over Kaena Ridge, Hawaii, *J. Phys. Oceanogr.*, *43*, 766–789.